



# Comprehensive analysis control effect of faults on the height of fractured water-conducting zone in longwall mining

Xianhui Wang<sup>1,2</sup> · Shuyun Zhu<sup>1,2</sup> · Haitao Yu<sup>1,2</sup> · Yanxin Liu<sup>3</sup>

Received: 7 November 2020 / Accepted: 24 April 2021 / Published online: 9 May 2021  
© The Author(s), under exclusive licence to Springer Nature B.V. 2021

## Abstract

In order to examine the height of a fractured water-conducting zone due to the presence of a fault, a typical working face in the Baodian Coal Mine which is located in the Yanzhou Coalfield of northeastern China is examined as a case study. Two subsurface conditions with and without a fault are considered. In this study, equations are developed to calculate the maximum span of the unsupported roof with and without the presence of a fault. Numerical models are used to examine the changes in stresses and the development of a plastic zone at different stages of mining. A comparison of the results based on theoretical analysis and numerical model shows that the height of the fractured water-conducting zone increases significantly with the presence of a fault. The height of the fractured water-conducting zone is about 1.50 times higher than the case without a fault. The results provide important insight into the prevention and control of water inrush in mines with thick and loose deposits and a thin bedrock.

**Keywords** Fault · Height of fractured water-conducting zone · Overburden failure model · Theoretical calculation · Numerical simulation

## 1 Introduction

Coal mining destroys the structure of overlying strata, which causes the initiation, extension and coalescence of roof fractures and forms water-conducting fracture zones (Palchik 2003; Guo et al. 2012; Wu et al. 2021). In recent decades, researchers in both China and other parts of the world have developed various methods to examine the height of the fractured water-conducting zones (Fan et al. 2019; Tan et al. 2018; Zeng et al. 2020). Qian et al. (1994) made

---

✉ Shuyun Zhu  
shyzhuqiao@163.com

<sup>1</sup> Key Laboratory of Coalbed Methane Resources and Reservoir Formation Process of the Ministry of Education, China University of Mining and Technology, Xuzhou, Jiangsu Province 221116, People's Republic of China

<sup>2</sup> School of Resources and Geosciences, China University of Mining and Technology, Xuzhou, Jiangsu Province 221116, People's Republic of China

<sup>3</sup> Department of Geological Survey, Baodian Coal Mine, Yanzhou Coal Mining Company, Zoucheng 273500, People's Republic of China

advances in the mechanical analyses of faults which previously only considered the impacts of caving rock blocks and degree of pseudo-plasticity by using the Voussoir beam model. Xu et al. (2012) examined the influence of the location of the key stratum of the roof on the height of the fractured water-conducting zone and proposed a method to predict the height based on the location of this key layer. Majdi et al. (2012) interpreted the height of distressed zone and the combined height of the caving and fracturing zones above the mined panel roof induced due to longwall mining as equivalent, and described the mechanism of development of the height of this zone. With the development of computer technology, simulation softwares are used to simulate coal mining, calculate the displacement and tensile strain of the surface and stratum, and predict the distribution of ground fractures and water flowing fractures (Zhao et al. 2016; Sun et al. 2018; Zhang et al. 2018; Lu et al. 2015). The height of the mining-induced fractured zone in formations overlying the coal seam was studied based on the “three maps-two predictions” approach (Wu and Zhou 2008; Zeng et al. 2018). Tian et al. (2019) studied the movement of roof and the instability of coal pillar in the process of multi seam mining. Yang and Xia (2018) studied the overburden failure law and characteristics of strata pressure behaviors under the weak and weathered composite roof during coal mining.

Faults are a common geological structure which break the continuity of the coal seams and roof (Das et al. 2018); rocks in the fault zone are usually fissured with gouges on the sliding surface, which lead to the fracturing of the roof of the roadway in mines (Li and Wu 2019; Wang et al. 2016; Wu et al. 2020). This results in the development of roof fissures near the fault in the working face with increased deformation and movement of the overlying strata. This situation not only creates difficulties while mining, but also poses hidden risks to the safety of miners at the mine surface (Wang and Meng 2018; Cui et al. 2018; Wang et al. 2019a, b). Mining-induced stress distribution and roof roadway deformation mechanisms during fault population activation were investigated by both theoretical analysis and 3D numerical simulations (Sun et al. 2019; Wang et al. 2016; Huang et al. 2021). Islam and Shingo (2009) used the boundary element method to numerically model the fault areas based on the Mohr–Coulomb failure criterion to analyze the safety of the mine. Naoi et al. (2015) recorded acoustics emissions to monitor the cracks in faults in a mine in South Africa and analyze the stresses and strengths of the faults. However, there are few comparative studies based on different mine geological conditions. Therefore, one of the objectives of this study is to address this research gap through a case study based on the geological conditions of working face 83–02 in the Baodian coal mine to examine the fault structure in the mined area due to impacts of coal seams after the completion of mining. Baodian Coal Mine is located in the Yanzhou Coalfield, in the Shandong Province of northeastern China. A mechanical model of the overburden failure will be developed to examine the mechanisms behind the changes and collapse of roofs with and without the presence of a fault at the working face. The height of the fractured water-conducting zone formed by the collapse of the roof with and without the presence of a fault caused by mining of the top coal seam is theoretically calculated and compared with the result obtained through numerical simulations.

## 2 Overview of the studied area

### 2.1 Overview of working face 83–02

The length of working face 83–02 in the Baodian Coal Mine along the strike and dip ranges from 1979 to 2505 m and 157 to 282 m, respectively, and the elevation at the

bottom of the floor ranges from 143 to 285 m below sea level. The coal seam mined in the working face, which is called the No. 3 Coal Seam, is generally influenced by the Xingxing Anticline and Yanzhou Syncline. Working face 83–02 is located in the center of the Xingxing Anticline with the Yanzhou Syncline to the north. The coal seam mined in the working face consists of the upper part of the No. 3 Coal Seam and the No. 3 Coal Seam itself in the Shanxi Formation. The upper part of the No. 3 Coal Seam, which has a thickness that ranges from 3.69 to 7.76 m with an average thickness of 5.28 m, is primarily the exploited seam.

Figure 1 shows the plan view of the fault distribution in working face 83–02. There are three faults to the south of the working face, which are labeled as VIII-F14, VIII-F15, and VIII-F72. VIII-F14 and VIII-F15 are located on the west side of the open cut. VIII-F6 is located near the south end of the No. 1 exploration roadway, with a fault throw (H) of 9.6 m. The strike of the fault is approximately north–south and parallel to the roadway. Two regular faults, VIII-F7 and VIII-F9, are found with fault throw of 1.3 m and 2.5 m, respectively. VIII-F76 is found in the middle of the No. 1 Roadway, and its strike is approximately north–south, and parallel to the fractured zone of the working face. Both faults, VIII-F6 and VIII-F76, have great impacts on the stability of the roadway in transporting people and materials. Faults VIII-F1 and VIII-F2 are found near the design stop line at the north end of the No. 1 Roadway, with minimal reduction in height and little influence on tunnel excavation. Faults VIII-F70, VIII-F44 and VIII-F43 are successively located along the No. 2 Roadway from south to north. Fault VIII-F42 is located near the design stop line, with a fault throw of 2 m.

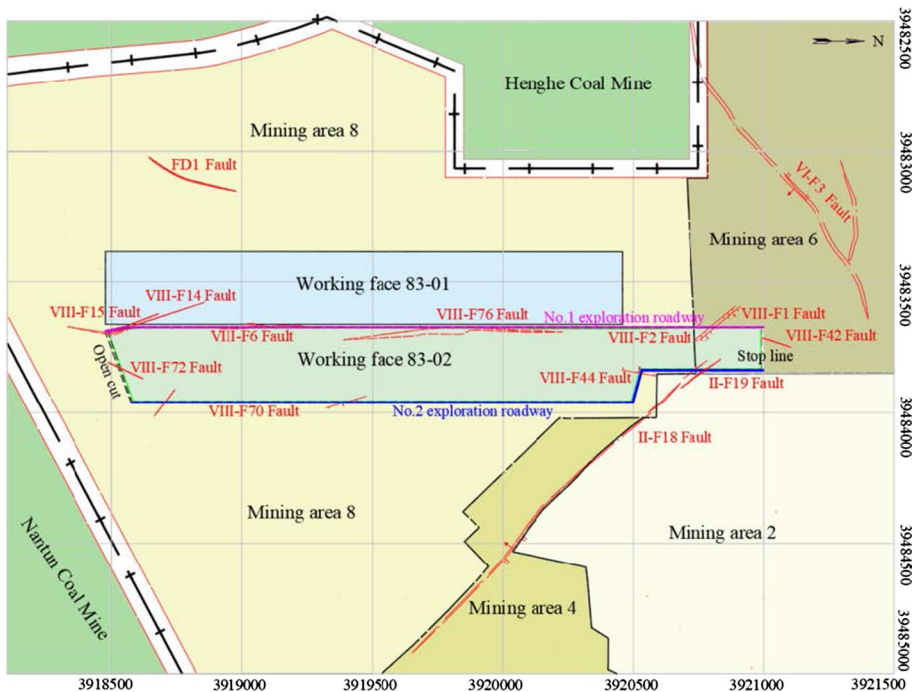


Fig. 1 Plan view of fault distributions of Working Face 83–02

Fault VIII-F76 is the largest fault in the entire working face, which is located under a thin layer of bedrock in the middle of the roadway. This fault has a large impact on the fractured zone of working face 83–02. Therefore, it is important to study the development of the height of the fractured water-conducting zone in the mine roof strata during the mining of the working face which is attributed to the existence of VIII-F76.

## 2.2 Overview of fault VIII-F76

Two large-scale drilling programs were carried out on this site with a total of eight groups of exploratory boreholes. In the first drilling program, five groups of exploratory boreholes were drilled in different locations perpendicular to the direction of the roadway facing the working face. The five groups of boreholes are labeled as Boreholes 1–1 to 1–5. In the second drilling program, three groups of exploratory boreholes were drilled, which were also perpendicular to the direction of the roadway and faced the working face. They are labeled as Boreholes 2–1 to 2–3 (Fig. 2). In total, twenty-five boreholes were drilled in eight groupings to determine the spatial distribution of the fault zones. Fault VIII-F76 is medium in size and a normal fault with a maximum fault throw of 13.6 m based on the exploratory drilling data during the construction of the roadways. The borehole information and the properties of VIII-F76 are summarized in Table 1.

## 3 Stress analysis of roof strata during mining on working face 83–02

### 3.1 Subsurface stratigraphies

Based on the observed geological conditions, two subsurface stratigraphies, with and without the presence of a fault, were developed to calculate the stress state of the roof of the working face and the height of fractured water-conducting zone.

The roof and floor of the No.3 Coal Seam are made up of six geological formations which include: Loose layer, silty sandstone, fine sandstone, aluminum mudstone, siltstone layers, and the coal seam. The coal seam itself consists of a total of seventeen layers. The height of the upper seam of the No. 3 Coal Seam is equal to 5 m, where the roof and floor are made up of a total of 12 and 4 layers of rock, respectively. The mechanical properties of each rock and coal layers are shown in Table 2. Based on these properties, two simplified subsurface stratigraphies, with and without a fault, have been developed to assess the stability of the working face as shown in Fig. 3.

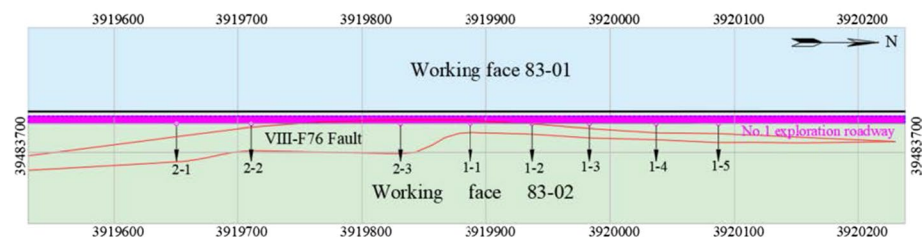
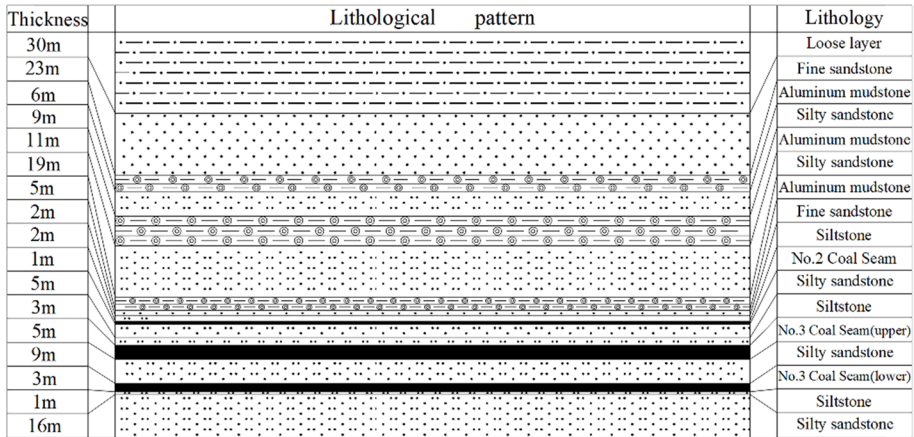
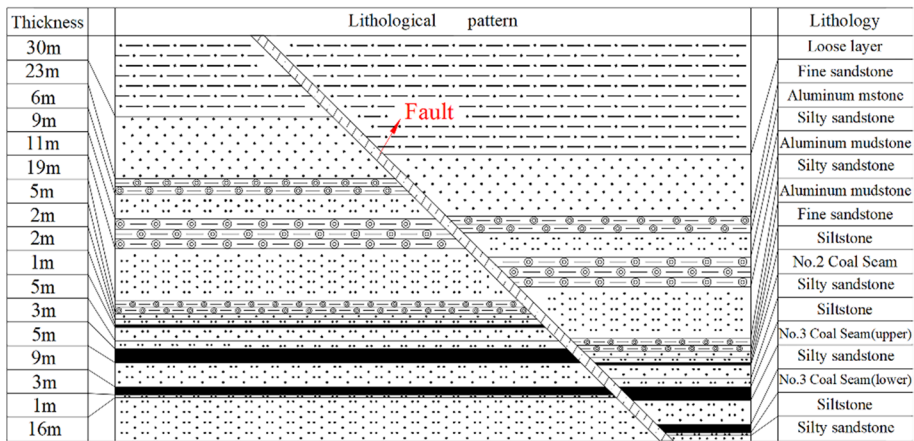


Fig. 2 Spatial distributions of exploratory boreholes in VIII-F76



(a) Subsurface stratigraphy – without presence of fault



(b) Subsurface stratigraphy with presence of fault

**Fig. 3** Two subsurface stratigraphies of Working Face 83–02. **a** Subsurface stratigraphy – without presence of fault **b** Subsurface stratigraphy with presence of fault

**Table 1** Summary of the properties of VIII-F76

Obs. Borehole	Number of boreholes	Cumulative drilling distance (m)	Fault orientation (°)	Fault dip angle (°)	Fault throw (m)
1–1	2	33.10	276	39	7.50
1–2	3	92.87	272	42	7.00
1–3	4	113.00	272	48	5.50
1–4	3	63.72	272	46~54	4.70
1–5	3	131.65	272	50	8.50
2–1	4	130.36	276	13~36	8.00
2–2	4	111.80	276	36	13.60
2–3	2	80.00	276	19~36	12.40

### 3.2 Calculation of maximum roof span

#### (1) Calculation of maximum roof span without fault.

During the initial cut of working face 83–02, there was the first sign of a roof collapse. Since the strength of the roof is relatively high, a hanging roof was developed without a total collapse. Since working face 83–02 is larger than the span of the hanging roof, the hanging roof can be considered as a fixed beam supported by the coal wall at one end of the working face and coal pillar at the other end. The weight of the overlying strata can be considered as the load acting on the beam (Qian and Liu 1984). The longitudinal section and stress analysis for calculating the roof span to prevent roof collapse by using a simplified model based on a fixed beam is shown in Fig. 4.

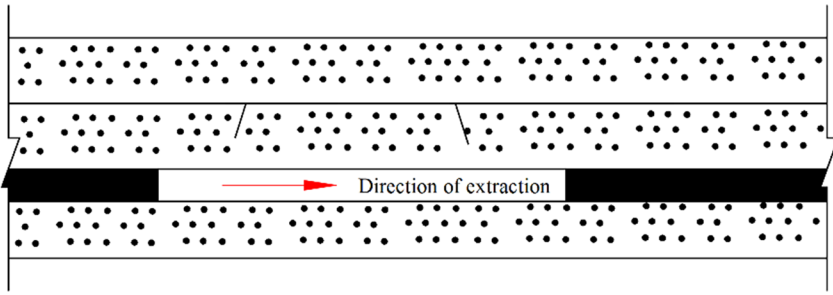
Based on a unit width in the third dimension of the fixed beam as shown in Fig. 4 b, the reaction forces,  $F_A$  and  $F_B$ , at both ends of the beam, are equal to each other due to symmetry. The bending moments,  $M_1$  and  $M_2$ , are also equal to each other due to symmetry, which can be calculated based on the beam theory. Since the net resultant vertical force in the rock mass is equal to zero, and  $F_A = F_B$ , each force should be equal to one half of the total load, that is:  $qL/2$ . The maximum bending moment at both ends of the fixed beam (Li et al. 2015) is equal to  $qL^2/12$ .

The normal bending stress at any point on the beam is:

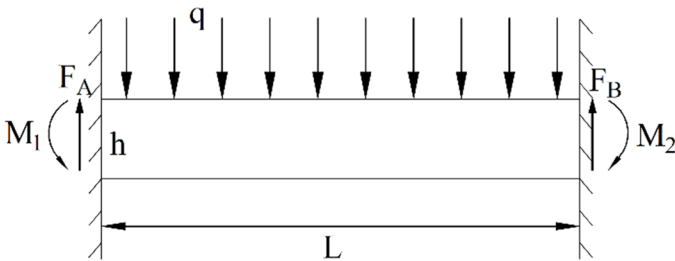
**Table 2** Calculation parameters of strata and fault

Geological Stratum	Thickness (m)	E (MPa)	$R_T$ (MPa)	$\gamma$ (kN/m <sup>3</sup> )	C (MPa)	$\varphi$ (°)
Loose layer	30	450	0.1	18,000	0.05	20
Fine sandstone	23	1100	2.5	23,520	3.40	31
Aluminum mudstone	6	660	1.6	20,580	2.00	27
Silty sandstone	9	1200	2.7	24,500	4.40	30
Aluminum mudstone	11	660	1.6	20,580	2.00	27
Silty sandstone	19	1200	2.7	24,500	4.40	30
Aluminum mudstone	5	660	1.6	20,580	2.00	27
Fine sandstone	2	1100	2.5	23,520	3.40	31
Siltstone	2	860	2.4	22,540	3.00	27
Coal (No.2 Coal Seam)	1	400	0.6	13,720	0.80	22
Silty sandstone	3	1200	2.7	24,500	4.40	30
Siltstone	5	860	2.4	22,540	3.00	27
Coal (upper seam; No.3 coal seam)	5	400	0.6	13,720	0.80	22
Silty sandstone	9	1200	2.7	24,500	4.40	30
Coal (lower seam; No.3 coal seam)	3	400	0.6	13,720	0.80	22
Siltstone	1	860	2.4	22,540	3.00	27
Silty sandstone	16	1200	2.7	24,500	4.40	30
Fault	–	600	0.4	19,600	0.80	20

Notes: E is the elastic modulus (MPa),  $R_T$  is the tensile strength (MPa),  $\gamma$  is the unit weight (kN/m<sup>3</sup>), C is the cohesion (MPa), and  $\varphi$  is the angle of internal friction (°)



(a) Longitudinal vertical section of mine strata



(b) Stress analysis of rock stratum based on simplified fixed beam model

**Fig. 4** Schematic and simple model for limiting overhanging. **a** Longitudinal vertical section of mine strata **b** Stress analysis of rock stratum based on simplified fixed beam model

$$\sigma = \frac{M \cdot y}{J_z} \tag{1}$$

where  $\sigma$  is normal bending stress (MPa) on any section of the beam,  $M$  is the bending moment of the section (kN·m),  $y$  is the distance from the normal bending stress point to the neutral axis of the section, and  $J_z$  is the moment of inertia of the section about the neural axis ( $m^4$ ).

The moment of inertia on the beam section ( $J_z$ ) is equal to:

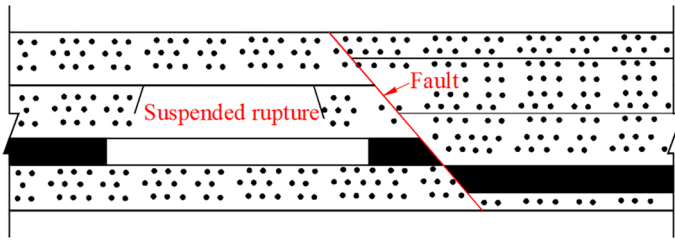
$$J_z = \frac{1}{12}h^3 \tag{2}$$

where  $h$  is the thickness of the rock layer (m) considering a beam of unit width in the third dimension.

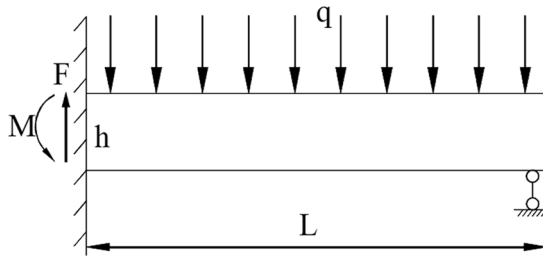
Substituting the bending moment of the beam of  $qL^2/12$  in Eq. (1), the maximum normal bending stress ( $\sigma_{max}$ ) is:

$$\sigma_{max} = \frac{qL^2}{2h^2} \tag{3}$$

When  $\sigma_{max} = R_T$ , the maximum span of the roof,  $L_{TT}$ , can be calculated from Eq. (3) as:



(a) Vertical section of mine with working face approaching a fault



(b) Stress analysis of simplified model of rock as beams

**Fig. 5** Stress analysis of rock layers and simplified model of rock as beams in working face before approaching fault. **a** Vertical section of mine with working face approaching a fault. **b** Stress analysis of simplified model of rock as beams

$$L_{T1} = h_i \cdot \sqrt{\frac{2R_T}{q_i + k_i}} \tag{4}$$

where  $q_i$  is the load acting on the beam (kN/m),  $R_T$  is the ultimate tensile strength of the rock (MPa),  $h_i$  is the thickness of the rock layer  $i$  (m), and  $k_i$  is the self-weight load of the rock layer  $i$  (kN/m).

The above calculation is applicable for a single beam or a single layer of rock. For multiple layers of rock above the coal seam, the maximum span can be calculated by considering an equivalent distributed overburden load from:

$$q_i = \frac{E_i h_i^3 (\gamma_i h_i + \gamma_{i+1} h_{i+1} + \dots + \gamma_n h_n)}{E_i h_i^3 + E_{i+1} h_{i+1}^3 + \dots + \gamma_n h_n^3} \tag{5}$$

where  $q_i$  is the load supported by the beam  $i$  (kN/m),  $E_i$  is the elastic modulus of the rock layer  $i$  (GPa),  $k_i$  is the self-weight load of the rock layer  $i$  (kN/m), and  $\gamma_i$  is the unit weight of the rock layer  $i$  (kN/m<sup>3</sup>).

(2) Calculation of maximum roof span with fault.

When the working face is close to a fault and the collapse of the roof falls into the goaf, as shown in Fig. 5 (a), the broken rock no longer transfers the horizontal force in the mining direction due to the deformation of the roof. The vertical force is mainly



**Fig. 6** Simplified mechanical model and stress analysis of rock stratum

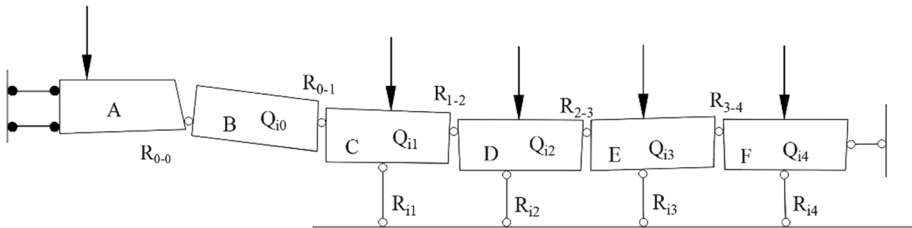
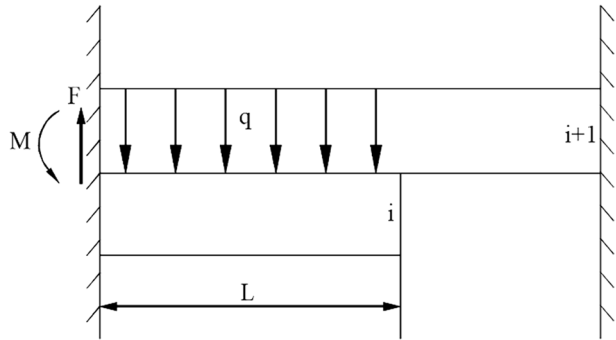


**Fig. 7** Model of Voussoir beams simplified into rock layers

supported by the coal seam in front of the goaf and the working face, which reduces the length of the intact roof and increases the height of the fractured zone.

The simplified model of the rock layer in the roof is shown in Fig. 5 (b). The beam in this figure is a statically indeterminate structure with one end constrained by the fixed rock mass and the other end supported by the coal seam.

When tensile failure occurs,  $\sigma_{max} = R_T$ , and the maximum span of the beam,  $L_{T2}$ , is:

$$L_{T2} = \frac{2h_i}{3} \sqrt{\frac{3R_T}{q_i + k_i}} \tag{6}$$

### 3.3 Calculation of maximum overhanging roof span

After collapse, one end of the rock layer in the roof is fixed and the other end is overhanged over the broken rock mass, thus forming a cantilever beam as shown in Fig. 6.

The maximum bending moment of the cantilever beam occurs at the fixed end A which is equal to  $qL^2/2$ . By substituting this maximum bending moment in Eq. (1), the maximum tensile stress in the beam at Point A is equal to  $3qL^2/h^2$ .

When tensile failure occurs,  $\sigma_{max} = R_T$ , and the maximum span of the beam,  $L_s$ , is:

$$L_s = h_i \sqrt{\frac{R_T}{3(q_i + k_i)}} \tag{7}$$

According to Eqs. (4), (6), and (7), the maximum roof span with and without a fault is calculated according to the parameters in Table 2 The results are shown in Table 3

### 3.4 Stability calculation of fractured rock block after collapse

When the mine face loses the support of the coal seam after the coal has been mined and the roof span is larger than the maximum span for stability, the surrounding rock of the roof will break and collapse. The rock layer may break and form an orderly arrangement of fault blocks much like a beam (Qian et al. 1994), which in essence is an arch or Voussoir beam. A simplified mechanical model of the blocks is shown in Fig. 7.

According to the theory of the Voussoir beam, the beam structure of roof blocks in the goaf is formed by block rotation above the upper wall goaf and extension of the block above the coal pillar. Half of the load of the rotating block above the goaf is supported by friction between the blocks, and the remaining load is transferred to the unmined pillar and to the fault in front by compression between the broken blocks.

Considering the interaction between two blocks as shown in Fig. 8, the horizontal force,  $T_i$ , at the interface is given by:

$$T_i = \frac{L_{ij}G_{ij}}{2(h_i - w_{ij})} \tag{8}$$

where  $L_{ij}$  (m) is the length of the block j of layer i,  $G_{ij}$  (kN) is the weight of the block j,  $w_{ij}$  (m) is the vertical deformation of the block j, and  $h_i$  is the thickness of the layer i.

When a rock layer is fractured, a fracture surface is formed which makes an angle  $\theta$ , with respect to the vertical as shown in Fig. 8.

When instability occurs at the fracture surface, the frictional resistance is less than the shear force on the fracture surface which can be expressed as:

$$(T \cos \theta - R \sin \theta) \cdot \text{tg}\varphi \leq R \cdot \cos \theta + T \cdot \sin \theta \tag{9}$$

$$T \cdot \sin(\phi - \theta) \leq R \cos(\phi - \theta) \tag{10}$$

where R (kN) is the vertical force at the contact and  $\varphi$  ( $^\circ$ ) is the friction angle at the contact.

**Table 3** Maximum roof span of rock layers

Geological Stratum	Thickness (m)	$L_{T1}$ (m)	$L_{T2}$ (m)	$L_S$ (m)
Loose layer	30	17.96	14.66	7.33
Fine sandstone	23	55.54	45.35	22.68
Aluminum mudstone	6	30.15	24.62	12.31
Silty sandstone	9	42.11	34.39	17.20
Aluminum mudstone	11	38.87	31.73	15.87
Silty sandstone	19	50.08	40.89	20.44
Aluminum mudstone	5	27.57	22.51	11.26
Fine sandstone	2	20.55	16.78	8.39
Siltstone	2	20.59	16.81	8.41
Coal (No.2 Coal Seam)	1	9.35	7.64	3.82
Silty sandstone	3	32.28	26.36	13.18
Siltstone	5	23.54	19.22	9.60

**Fig. 8** Force diagram of block interaction

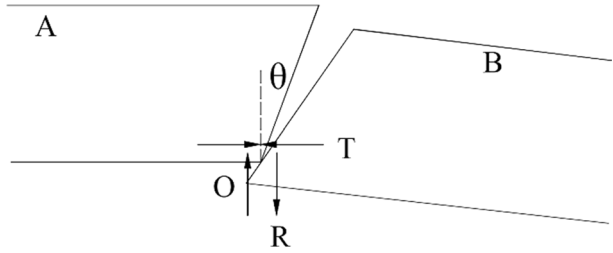
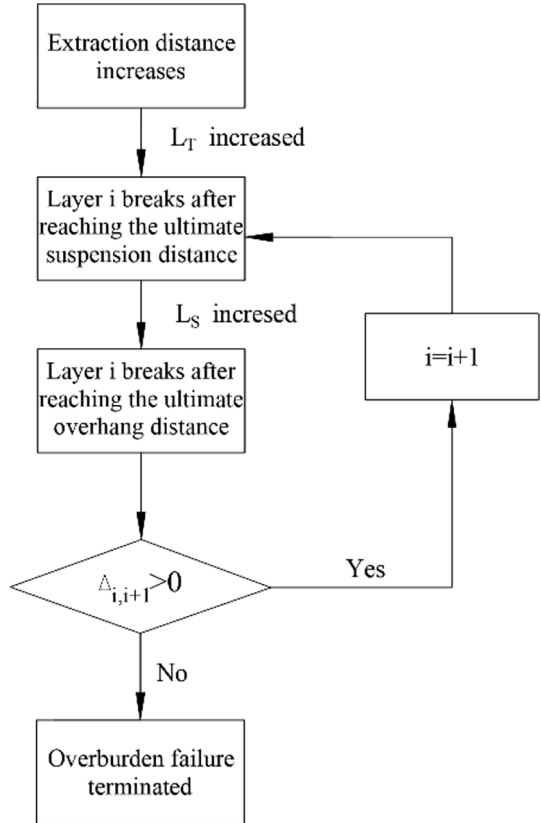


**Fig. 9** Flowchart of roof overburden failure analysis



When the shear force between the rock blocks is greater than the friction force, the Voussoir beam becomes unstable:

$$R \geq Ttg(\varphi - \theta) \tag{11}$$

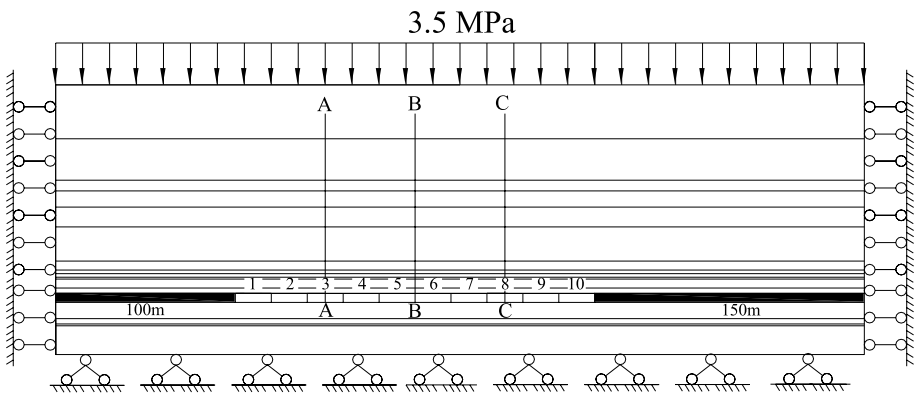
By substituting Eq. (8) in Eq. (11), the maximum length of the block can be calculated from:

$$L_{ij} \leq \frac{2(h_i - w_{ij})}{tg(\varphi - \theta)} \tag{12}$$

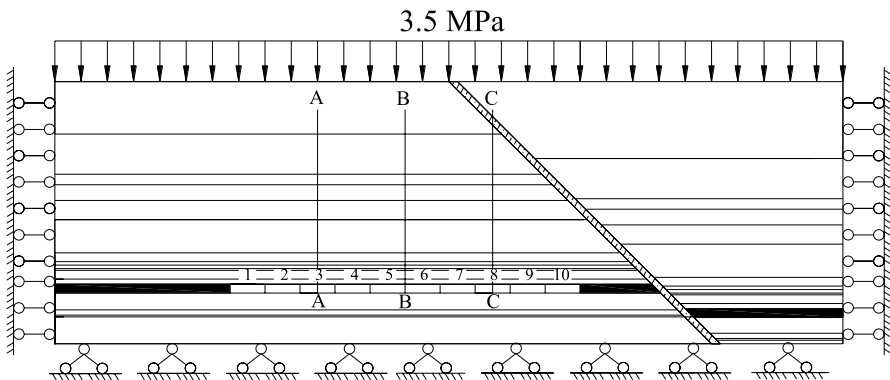
When a rock block in the Voussoir beam meets the criterion in Eq. (12), the structure becomes unstable. Guo et al. (2019) developed an overburden failure model for fully mechanized caving mining to explain the mechanism of the initial caving of the rock strata above the goaf, failure of the overhanging roof strata and instability of the rock blocks. The flowchart of the model is shown in Fig. 9.

With the advance of the working face, if the total distance to layer  $i + 1^{\text{th}}$  is less than the maximum distance for stability consideration based on the Voussoir beam, the rock layer is in a stable state. In this case, the separation distance between layer  $i^{\text{th}}$  and layer  $i + 1^{\text{th}}$  is equal to:

$$\Delta_{i,i+1} = m - \sum_{i=1}^i h_i(K_p - 1) \tag{13}$$



(a) Schematic diagram of boundary conditions of no-fault model



(b) Schematic diagram of boundary conditions of fault model

**Fig. 10** Schematic diagram of initial conditions and boundary conditions of two numerical models. **a** Schematic diagram of boundary conditions of no-fault model **b** Schematic diagram of boundary conditions of fault model

where  $\Delta_{i,i+1}$  is the separation distance between the  $i$ th layer and the  $i + 1$ th layer (m),  $m$  is the thickness of the coal seam (m),  $K_p$  is the residual crushing coefficient, and  $h_i$  is the thickness of the  $i$ th layer (m).

When the separation distance is less than zero, the instability of the  $i$ th layer will not affect the stability of the  $i + 1$ th layer, and the fractured zone will cease to develop. The  $i$ th rock layer above the coal seam becomes unstable and forms a fractured water-conducting zone. The height of the fractured zone,  $H$ , can be calculated from:

$$H = \sum_{i=1}^i h_i K_p \tag{14}$$

According to the study by Guo et al. (2002), the crushing coefficient mainly depends on the pore size of the material between the rock blocks in a loose state. Particle size and surface roughness play an important role for the crushing coefficient; that is, the smaller the particle size of the broken pieces, the larger the crushing coefficient, which can be expressed as:

$$K_p = K_z - 0.017 \ln d \tag{15}$$

where  $K_p$  is the residual crushing coefficient,  $K_z$  is the crushing coefficient of the roof and  $d$  (m) is the distance between the rock layer and the coal seam.

The roof of the No. 3 coal seam is a layer of siltstone with a crushing coefficient of 1.15. According to Eq. (13), the separation distance between successive layers of rock and the thickness of each layer are calculated and summarized in Table 4.

According to Eq. (14), the height of the fractured water-conducting zone at the working face without a fault is determined to be 67.8 m, and the height with a fault is equal to 100.9 m.

**Table 4** Separation distance and height of fractured zone

Geological Stratum	Without a Fault		With a Fault	
	$\Delta_{i,i+1}$ (m)	$h_i K_p$ (m)	$\Delta_{i,i+1}$ (m)	$h_i K_p$ (m)
Loose layer	–	–	0	10.3
Fine sandstone	< 0	–	0.40	23.92
Aluminum mudstone	0.12	6.60	1.32	6.24
Silty sandstone	0.54	9.54	1.56	9.36
Aluminum mudstone	1.34	12.10	1.92	11.55
Silty sandstone	2.44	20.14	2.47	20.14
Aluminum mudstone	3.58	5.50	3.61	5.3
Fine sandstone	4.08	2.12	3.91	2.12
Siltstone	4.20	2.12	4.03	2.12
Coal (No.2 Coal Seam)	4.32	1.20	4.15	1.07
Silty sandstone	4.52	5.30	4.22	5.45
Siltstone	4.82	3.18	4.67	3.33

## 4 Numerical model of the fractured zone at the working face

### 4.1 Modeling scheme and boundary conditions

To study the influence of faults on the stability of the working face, two numerical models, with and without the presence of a fault, have been developed for the subsurface stratigraphies in Fig. 3. The size of the model is a 450 m × 300 m × 150 m (X × Y × Z) block with an average thickness of the coal seam of 5 m. There are 12 layers of rock above the coal seam with a total height of 116 m. Below the coal seam, there are 4 layers of rock with a total height of 29 m. The thickness of the overburden material above the model is about 140 m. This gives an equivalent vertical overburden pressure of 3.5 MPa which is applied uniformly on the upper boundary of the model (see Fig. 10). The lower boundary condition of the model is assumed to be fixed with a zero displacement boundary condition in all three directions. For the left and right boundaries of the model which are adjacent to the solid rock, vertical roller boundaries are imposed which allow movement only in the vertical direction.

The three-dimensional models that show the layers of the material are provided in Fig. 11.

Model 1 has a total of 112,500 zones and 120,156 nodes, and Model 2 has 101,250 zones and 108,376 nodes. To examine the changes in stress at the roof due to the excavation of the coal seam, three monitoring lines located at 50 m, 100 m and 150 m in the x direction (see Fig. 10) have been set up for both models. The lines are denoted as A, B, C, and A', B', C' for Models 1 and 2, respectively; see Fig. 10. The Mohr–Coulomb model is used to model the constitutive response of the rock.

The model parameters are given in Table 2. A commercial software, FLAC<sup>3D</sup>, was used in this simulation. Referring to Fig. 10, the coal seam has a thickness of 5 m with a width of 100 m. The length of the working face is 200 m for both models. Modeling the excavation of the coal seam in Model 1 starts at an X value of 100 m with a width of 100 m in the Y direction. The excavation for both models is modeled in 10 steps with a 20 m excavation in each step with removal of the entire coal layer in each step. The total length of excavation of the coal seam in the X direction is 200 m. After the excavation, there is 100 m of coal pillar at both ends of the working face. There is no additional support for the roof which can cave into the excavation freely (Fig. 12).

### 4.2 Results of the numerical model

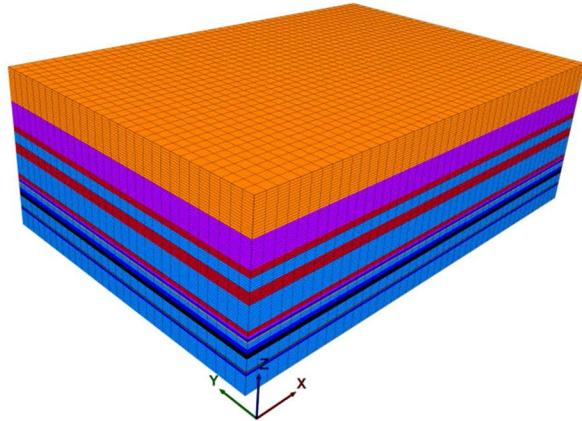
#### (1) Effects of working face mining on plastic zone development in the rock.

Figures 12 a, b show the calculated plastic zones at the completion of mining of Models 1 and 2, respectively.

In simulating the mining of the working face, stresses in the overburden strata are changed and plastic zones are formed at the north and south ends of the working face. Based on the properties of the rock and the constitutive response of the material, the changes in the plastic zones are calculated. Since the plastic zones represent plastic yielding of the rock which results in significant damage to the material, the hydraulic conductivity of the rock mass will likely be increased. Therefore, the size of the plastic

**Zone**

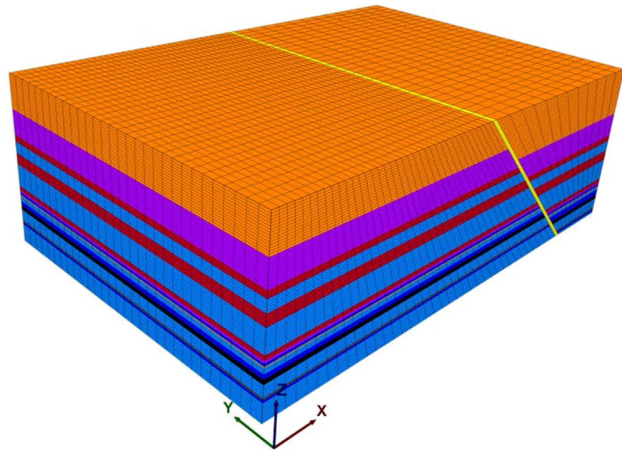
- Colorby: Group Any
- Aluminum-Mudstone
  - Fine-Sandstone
  - Loose-Sediment
  - No.2-Coal-Seam
  - No.3-Coal-Seam-lower
  - No.3-Coal-Seam-upper
  - Siltstone
  - Slity-Sandstone



**(a) Model 1 without fault**

**Zone**

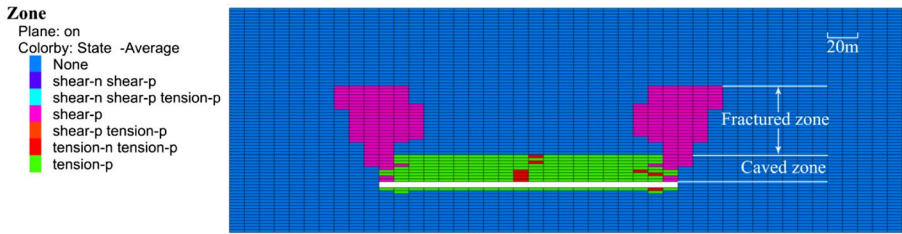
- Colorby: Group Any
- Aluminum-Mudstone
  - Fault
  - Fine-Sandstone
  - Loose-Sediment
  - No.2-Coal-Seam
  - No.3-Coal-Seam-lower
  - No.3-Coal-Seam-upper
  - Siltstone
  - Slity-Sandstone



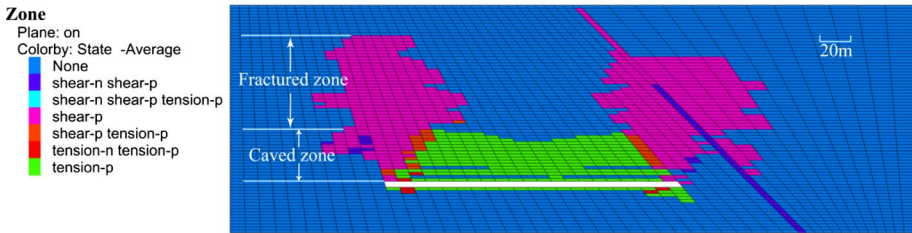
**(b) Model 2 with fault**

**Fig. 11** Numerical models for fractured zone analysis. **a** Model 1 without fault. **b** Model 2 with fault

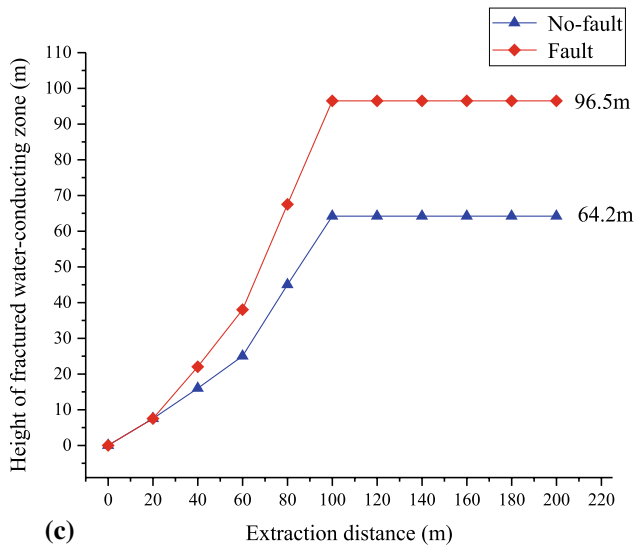
zone is considered to be the size of the fractured water-conducting zone. As shown in Fig. 12, at the completion of the working face for the case without a fault, the plastic zone shows a “saddle-shaped” failure with more shear yielding at the north and south ends and tensile yielding in-between. The maximum height at both sides of the plastic zone is about 64.2 m which is considered to be the height of the fractured water-conducting zone. For the case with a fault, the plastic zone near the fault region and the yielding of the fault are joined together. The plastic zones resemble a more “irregular saddle” shape with increase in the plastic zone at the south side of the working face at the beginning of the mining. The height of the plastic zone at both ends is about 96.5 m which is considered to be the height of the fractured water-conducting zone. In this case, it is about 1.50 times higher than the case with no fault. Therefore, in the case with



(a) Final distribution of plastic zone of Model 1



(b) Final distribution of plastic zone of Model 2



(c)

**Fig. 12** Calculated plastic zones and height of fractured water-conducting zone for two models. **a** Final distribution of plastic zone of Model 1 **b** Final distribution of plastic zone of Model 2 **c** Height of water fractured zone for Model 1, without fault, and Model 2, with fault

a fault, the height of the roof failure is obviously higher than that without a fault. The influence of a fault on the stability of the surrounding rock is evident.

(2) Effects of the working face mining on the stresses in the roof.



Mining of the coal seam changes the in-situ stresses with stress redistribution in the rock. The existence of faults will have an impact on stress redistribution and stress changes, etc. Therefore, it is important to study the changes in stresses in the rock and the development of the fractured water-conducting zone due to the faults by using numerical modeling.

The initial vertical stress states, with and without faults, of the rock are shown in Fig. 13 a and b. It can be seen that the initial and final stress fields in the rocks are affected by the presence of the fault. The stress field with the fault is complex in forming the fractured zone. As a result, the stresses are all reduced at the fault compared to the case without a fault. The stresses inside the fault are also changed with the maximum stresses at the bottom of the fault. It can be seen that the upper part of the fault above the long wall is subjected to tensile stresses which makes the upper part of the working face move along the fault. Moreover, due to the existence of the fault, the stress distribution in this stratum is non-uniform which presents a complex condition in excavating the coal seam. As seen in Fig. 13 c and d, there are stress concentrations at both ends of the working face in both cases. The maximum vertical stress in the case with no fault is equal to 14.4 MPa, and the maximum vertical stress in the case with a fault is equal to 14.7 MPa.

Figure 14 shows the vertical stress distribution along the 6 monitoring lines at different stages of mining of the working face.

As seen in Fig. 14, mining the working face leads to substantial changes in stress distributions. In Figs. 14 a and b, Monitoring Lines A-A and A'-A' are 200 m away from the fault, which is far away from the fault. There is no significant difference in vertical stress between roof without fault and fault. In Figs. 14 c and d, when mining of the working face approaches the vicinity of the fault at a distance of 150 m away from Monitoring Lines B-B and B'-B', the vertical stresses at the roof for the case without a fault and the case with a fault are significantly different. In Figs. 14 e and f, Monitoring Lines C-C and C'-C' are located at a distance of 50 m from the fault and Monitoring Line C'-C' intersects the fault. When excavation of the working face approaches the vicinity of the monitoring lines, the vertical stresses above the roof for the case without a fault are significantly different from the case with a fault, thus indicating that the presence of a fault has great influence on the changes in vertical stresses during mining of the working face which affects the development of the fractured water-conducting zone in the rock.

Figure S15 shows the vertical stresses in the roof at different stages of mining of the working face. The stresses in the roof of the mined area are low, and approach zero. The variation in the stresses in the roof along the working face is approximately parabolic in shape. The stresses at the front of the mined working face are higher than the stresses in the roof of the mined area. The pattern of the variations of stresses in the roof propagates forward with the advancement of the working face. In the case where there is no fault, there are two regions of stress concentration located at the two ends of the mined working face.

The vertical stress increases with the increase of the mining distance, and the variations of stresses are roughly symmetrical about the middle of the mined working face. In the case where there is a fault, there are three regions of stress concentrations located at both ends of the mined area and the fault zone. With progression of mining, the stress concentration region at the north end approaches the fault, thus intensifying the stress concentration at the fault.

### 4.3 Results and analysis

1. Summary of the results from the theoretical analysis and numerical modeling.

**Fig. 13** Vertical stress distributions in the rock due to mining. **a** Initial vertical stress contours with no fault. **b** Initial vertical stress contours with a fault. **c** Vertical stress contours at the completion of mining with no fault. **d** Vertical stress contours at the completion of mining with a fault

In the theoretical analysis, the equations to calculate the maximum span and the height of the fractured water-conducting zone are developed and combined with the stress state in the rock for the cases with and without a fault. The mechanical model is simplified in order to analyze the stress state due to mining. Based on the failure of the overburden material in the fully mechanized caving mining, the height of the fractured water-conducting zone for the case with and without a fault is 100.9 m and 67.8 m, respectively.

In numerical modeling, two three-dimensional numerical models have been developed for the cases with and without a fault. At the completion of mining, the stress distribution and plastic area in the rock are obtained. The height of the fractured water-conducting zone for the case with and without a fault is found to be 96.5 m and 64.2 m, respectively.

## 2. Interpretation of results

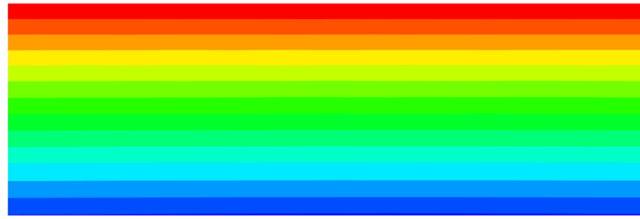
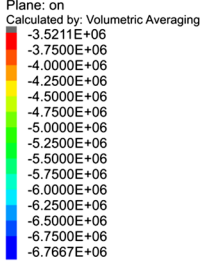
Based on mining theory, mining of the coal seam causes tensile failure, tensile fracture, shear failure, and elastic rock when moving away from the top of the coal seams into the rock strata. Shear yielding plastic zones develop at both ends of the goaf, and the roof in the middle of the goaf appears to yield partially in tension. As shown in Table 3 with the presence of a fault, the maximum span of the unsupported roof is significantly smaller than the case without a fault, which shows that the existence of a fault has a great impact on the stability and integrity of the rock. The results provided in Table 4 also show that the fractured water-conducting zone of the roof increases significantly with the presence of a fault.

In the numerical analysis, there are changes in the stress distribution and plastic zone due to mining. With the advance of the working face, the stresses in the roof are increasing, which lead to the gradual yielding of the roof and the formation of the fractured water-conducting zone. At both ends of the working face, stress concentrations develop in the roof and below the mine floor with rapid stress changes which lead to significant damages to the rock. It can be seen in Fig. 12 that in the case with a fault, the height of the failure zone in the roof is significantly higher than that without a fault, and the influence of the fault on the stability of the rock is evident. In Fig. 13, it can be seen that stresses are increasing in the mined area and in the coal wall at the ends for both cases. The maximum vertical stress in the case with no fault is equal to 14.4 MPa, and the maximum stress in the case with a fault reaches 14.7 MPa. The existence of a fault has a great influence on the change in vertical stress in the roof during the mining of the working face, which will further affect the development of the fractured water-conducting zone in the roof as shown in Figs. 14 and 15.

## 5 Conclusions

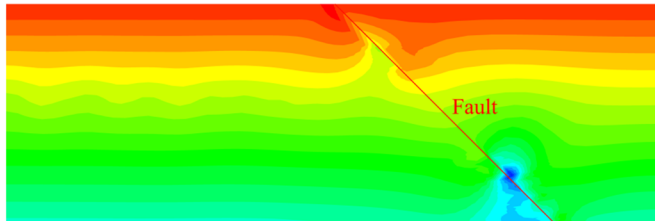
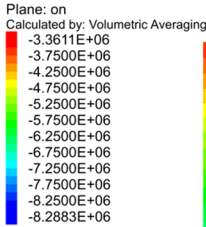
1. Based on a detailed analysis of the geological and hydrogeological conditions of the studied area, mechanical models for the case with and without a fault for Working Face 83–02 are developed. The maximum span and maximum overhanging distance of the mine roof are calculated based on the beam theory for the case with and without a fault. The heights of the fractured water-conducting zone with and without a fault are

**Contour of ZZ-Stress**



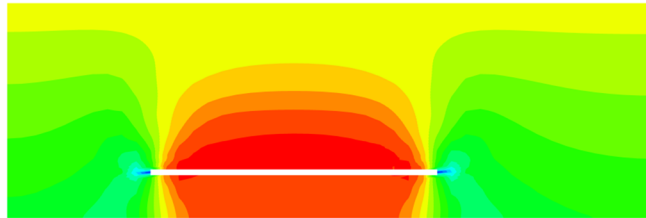
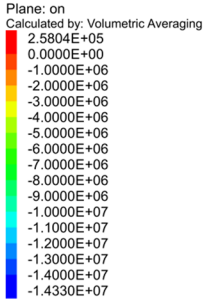
**(a)** Initial vertical stress contours with no fault

**Contour of ZZ-Stress**



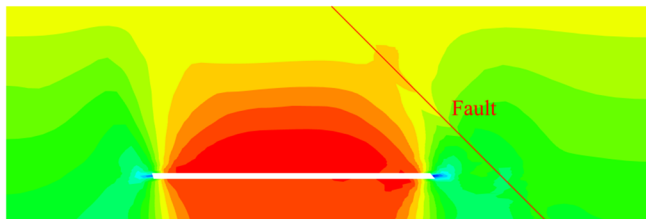
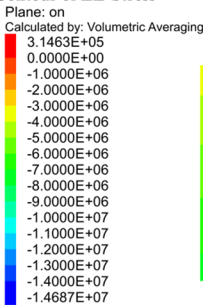
**(b)** Initial vertical stress contours with a fault

**Contour of ZZ-Stress**

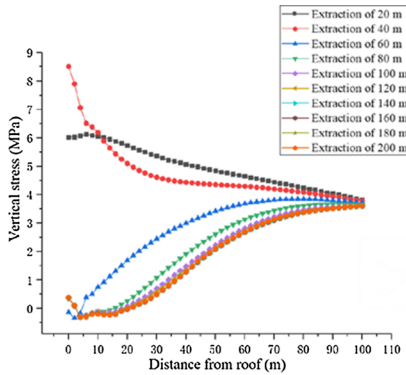


**(c)** Vertical stress contours at the completion of mining with no fault

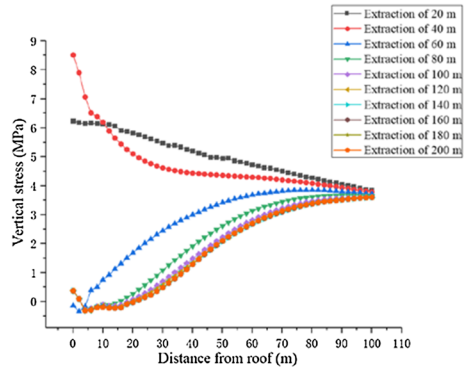
**Contour of ZZ-Stress**



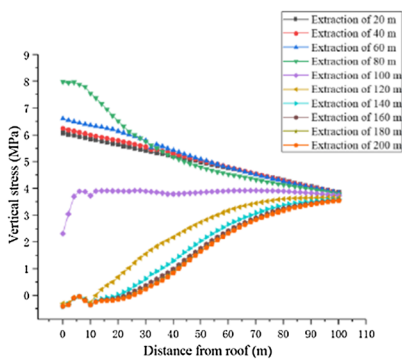
**(d)** Vertical stress contours at the completion of mining with a fault



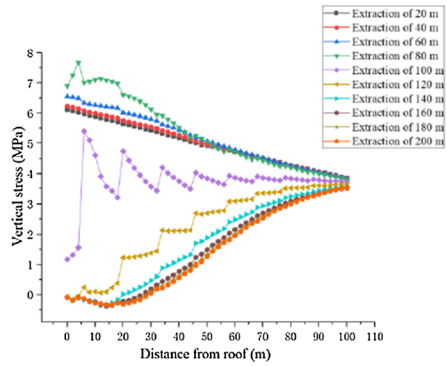
(a) Vertical stress along Monitoring Line A-A without a fault



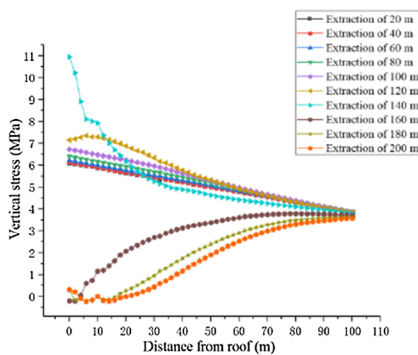
(b) Vertical stress along Monitoring Line A'-A' with a fault



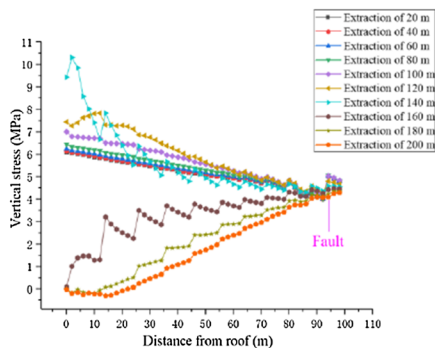
(c) Vertical stress along Monitoring Line B-B without a fault



(d) Vertical stress along Monitoring Line B'-B' with a fault



(e) Vertical stress along Monitoring Line C-C without a fault



(f) Vertical stress along Monitoring Line C'-C' with a fault

**Fig. 14** Vertical stress distributions along the monitoring lines for Models 1 and 2. **a** Vertical stress along Monitoring Line A-A without a fault **b** Vertical stress along Monitoring Line A'-A' with a fault **c** Vertical stress along Monitoring Line B-B without a fault **d** Vertical stress along Monitoring Line B'-B' with a fault **e** Vertical stress along Monitoring Line C-C without a fault **f** Vertical stress along Monitoring Line C'-C' with a fault

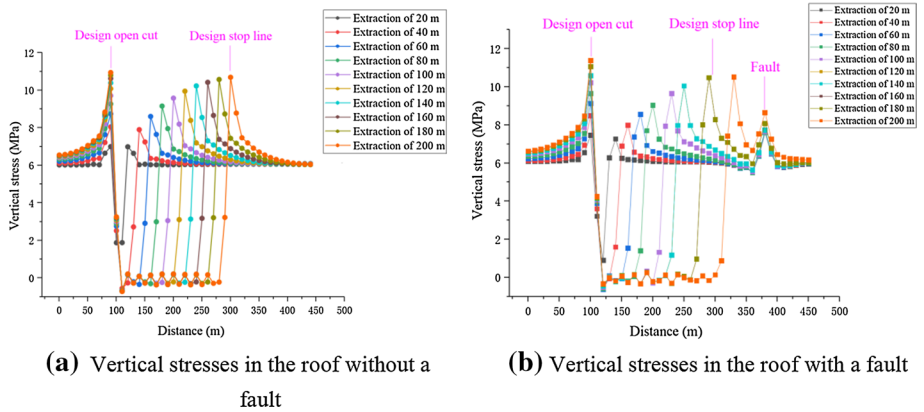


**Fig. 15** Vertical stresses in roof during mining of the working face. **a** Vertical stresses in the roof without a fault **b** Vertical stresses in the roof with a fault

calculated to be 100.9 m and 67.8 m, respectively. The height of the fractured water-conducting zone with a fault is about 1.48 times of that without a fault.

2. Three-dimensional numerical models are used to study the changes in stresses and plastic zones in the overburden material due to mining. By comparing the results in three monitoring lines located at different distances in the working face, it is found that the height of the fractured water-conducting zone increases significantly when the working face approaches the vicinity of the fault. The heights of the fractured water-conducting zone for the case with a fault and without a fault are simulated to be 96.5 m and 64.2 m, respectively. The height of the fractured water-conducting zone with a fault is about 1.50 times higher than that without a fault.
3. The results from the numerical model are consistent with those of the theoretical analysis. It is found that the height of the fractured water-conducting zone in the presence of a fault is significantly higher than that without a fault. In this case, the height of the fractured water-conducting zone with a fault is about 1.50 times higher than that without a fault.

**Acknowledgments** This research is supported by the Fundamental Research Funds for the Central Universities (Grant No. 2017CXNL03) and the Priority Academic Program Development of Jiangsu Higher Education Institutions.

**Author contributions** The manuscript was mainly written by Xianhui Wang under the guidance of Professor Zhu, the data in the manuscript is provided by Yanxin Liu, and the proofreading and collation of manuscripts is done by Haitao Yu.

**Funding** This research is supported by the Fundamental Research Funds for the Central Universities (Grant No. 2017CXNL03) and the Priority Academic Program Development of Jiangsu Higher Education Institutions (PAPD).

**Declarations**

**Conflict of interest** No conflict of interest exists in the submission of this manuscript, and manuscript is approved by all authors for publication. I would like to declare on behalf of my co-authors that the work described was original research that has not been previously published, is not currently submitted for review to any other journal, and will not be submitted elsewhere before a decision is made by this journal.

## References

- Cui FP, Wu Q, Lin YH, Zeng YF, Zhang KL (2018) Damage features and formation mechanism of the strong water inrush disaster at the Daxing Coal Mine, Guangdong Province. *China Mine Water Environ* 37(2):346–350. <https://doi.org/10.1007/s10230-018-0530-4>
- Das AJ, Mandal PK, Sahu SP, Kushwaha A, Bhattacharjee R, Tewari S (2018) Evaluation of the effect of fault on the stability of underground workings of coal mine through DEM and statistical analysis. *J Geol Soc India* 92(6):732–742. <https://doi.org/10.1007/s12594-018-1096-2>
- Fan KF, Li WP, Wang QQ, Liu SL, Xue S, Xie CY, Wang ZK (2019) Formation mechanism and prediction method of water inrush from separated layers within coal seam mining: A case study in the Shilawusu mining area, China. *Eng Fail Anal* 103:158–172. <https://doi.org/10.1016/j.engfailanal.2019.04.057>
- Guo GL, Miao XX, Zhang ZN (2002) Research on ruptured rock mass deformation characteristics of longwall goafs. *Sci Technol Eng* 2(5):44–47 (**In Chinese**)
- Guo H, Yuan L, Shen BT, Qu QD, Xue JH (2012) Mining-induced strata stress changes, fractures and gas flow dynamics in multi-seam longwall mining. *Int J Rock Mech Min* 54:129–139
- Guo WB, Zhao GB, Lou GZ, Wang SR (2019) A new method of predicting the height of the fractured water-conducting zone due to high-intensity longwall coal mining in China. *Rock Mech Rock Eng* 52(8):2789–2802. <https://doi.org/10.1007/s00603-018-1567-1>
- Huang Z, Zeng W, Wu Y, Li SJ, Gu QX, Zhao K (2021) Effects of temperature and acid solution on the physical and tensile mechanical properties of red sandstones. *Environ Sci Pollut R*. <https://doi.org/10.1007/s11356-020-11866-x3>
- Islam MR, Shinjo R (2009) Mining-induced fault reactivation associated with the main conveyor brlt roadway and safety of the Barapukuria Coal Mine in Bangladesh: Constraints from BEM simulations. *Int J Coal Geol* 79(4):115–130
- Li B, Wu Q (2019) Catastrophic evolution of water inrush from a water-rich fault in front of roadway development: a case study of the Hongcai coal mine. *Mine Water Environ* 38(2):421–430. <https://doi.org/10.1007/s10230-018-00584-z>
- Li N, Wang EY, Ge MC, Liu J (2015) The fracture mechanism and acoustic emission analysis of hard roof: a physical modeling study. *Arab J Geosci* 8(4):1895–1902. <https://doi.org/10.1007/s12517-014-1378-y>
- Lu YY, Song CP, Jia YZ, Xia BW, Ge ZL, Tang JR, Li Q (2015) Analysis and numerical simulation of hydrofracture crack propagation in coal-rock bed. *Compos Model Eng* 105(1):69–86
- Majidi A, Hassani FP, Nasiri MY (2012) Prediction of the height of distressed zone above the mined panel roof in longwall coal mining. *Int J Coal Geol* 98:62–72. <https://doi.org/10.1016/j.coal.2012.04.005>
- Naoi M, Nakatani M, Otsuki K, Yabe Y, Kgarume T, Murakami O, Masakale T, Ribeiro L, Ward A, Moriya H, Kawakata H, Durrheim R, Ogasawara H (2015) Steady activity of microfractures on geological faults loaded by mining stress. *Tectonophysics* 649:100–114. <https://doi.org/10.1016/j.tecto.2015.02.025>
- Palchik V (2003) Formation of fractured zones in overburden due to longwall mining. *Environ Geol* 44(1):28–38. <https://doi.org/10.1007/s00254-002-0732-7>
- Qian MG, Liu TC (1984) *Mine pressure and control*. Beijing: China Coal Industry Publishing House. pp 70–75
- Qian MG, Miao XX, He FL (1994) Analysis of key block in the structure of Voussoir beam in longwall mining. *J China Coal Soc* 6:557–563 (**In Chinese**)
- Sun W, Zahng Q, Luan YZ, Zhang XP (2018) A study of surface subsidence and coal pillar safety for strip mining in a deep mine. *Environ Earth Sci* 77(17):627–643. <https://doi.org/10.1007/s12665-018-7810-y>
- Sun WB, Xue YC, Li TT, Liu WT (2019) Multi-field coupling of water inrush channel formation in a deep mine with a buried fault. *Mine Water Environ* 38(3):528–535. <https://doi.org/10.1007/s10230-019-00616-2>
- Tan Y, Guo WB, Bai EH, Yang DM (2018) The height of fractured zones caused by strip Wongawilli mining in a shallow buried coal seam underlying a hard roof. *Curr Sci India* 115(7):1387–1392
- Tian CL, Yang XL, Sun HT, Liu YB, Hu QT (2019) Experimental study on the overburden movement and stress evolution in multi-seam mining with residual pillars. *Energy Sci Eng* 7(6):3095–3110
- Wang X, Meng FB (2018) Statistical analysis of large accidents in China's coal mines in 2016. *Nat Hazards* 92(1):311–325. <https://doi.org/10.1007/s11069-018-3211-5>
- Wang F, Xu JL, Xie JL, Li Z, Guo JK (2016) Mechanisms influencing the lateral roof roadway deformation by mining-induced fault population activation: a case study. *Int J Oil Gas Coal T* 11(4):411–428. <https://doi.org/10.1504/IJOGCT.2016.075115>
- Wang HW, Shi RM, Lu CS, Jiang YD, Deng DX, Zhang DQ (2019a) Investigation of sudden faults instability induced by coal mining. *Safety Sci* 115:256–264. <https://doi.org/10.1016/j.ssci.2019.01.019>

- Wang F, Xu JL, Xie JL (2019b) Effects of arch structure in unconsolidated layers on fracture and failure of overlying strata. *Int J Rock Mech Min* 114:141–152. <https://doi.org/10.1016/j.ijrmms.2018.12.016>
- Wu Q, Zhou WF (2008) Prediction of inflow from overlying aquifers into coalmines: a case study in Jinggezhuang Coalmine, Kailuan. *China Environ Geol* 55(4):775–780
- Wu Y, Huang Z, Zhao K, Zeng W, Gu QX, Zhang R (2020) Unsteady seepage solutions for hydraulic fracturing around vertical wellbores in hydrocarbon reservoirs. *Int J Hydrogen Energ* 45:9496–9503
- Wu Y, Huang Z, Xue S (2021) Effect of temperature on physical mechanical and acoustic emission properties of Beishan granite Gansu Province China. *Nat Hazards*. <https://doi.org/10.1007/s11069-021-04647-3>
- Xu JL, Zhu WB, Wang XZ (2012) New method to predict the height of fractured water-conducting zone by location of key strata. *J China Coal Soc* 37(05):762–769 ((In Chinese))
- Yang WF, Xia XH (2018) Study on mining failure law of the weak and weathered composite roof in a thin bedrock working face. *J Geophys Eng* 15(6):2370–2377. <https://doi.org/10.1088/1742-2140/aacedf>
- Zeng YF, Wu Q, Liu SQ, Zhai YL, Lian HQ, Zhang W (2018) Evaluation of a coal seam roof water inrush: case study in the Wangjialing coal mine. *China Mine Water Environ* 37(1):174–184
- Zeng W, Huang Z, Wu Y, Li SJ, Zhang R, Zhao K (2020) Experimental investigation on mining induced strain and failure characteristics of rock masses of mine floor. *Geomat Nat Haz Risk* 11(1):491–509
- Zhang GC, Liang SJ, Tan YL, Xie FX, Chen SJ, Jia HG (2018) Numerical modeling for longwall pillar design: a case study from a typical longwall panel in China. *J Geophys Eng* 15(1):121–134
- Zhao KY, Xu NX, Mei G, Tian H (2016) Predicting the distribution of ground fissures and water-conducted fissures induced by coal mining: a case study. *Springerplus* 5:977–1002

**Publisher's Note** Springer Nature remains neutral with regard to jurisdictional claims in published maps and institutional affiliations.